Supplemental Information: A Non-Empirical Model for Lithium Transport in Composite ASSB Cathodes, Validated by Operando Neutron Radiography

Andre Adam[a,b,†], Chanho Kim[a,†], Yuanshun Li[a,c], Yuxuan Zhang[d], Jean-Christophe Bilheux[d], Xianglin Li[b,e], Lei Cheng[a], Hassina Bilheux[d], and Guang Yang[a,f,*]

[a]Chemical Sciences Division, Oak Ridge National Laboratory, Oak Ridge, TN, USA
[b]Department of Mechanical Engineering, University of Kansas, Lawrence, KS USA
[c]Department of Chemical and Biomolecular Engineering, University of Tennessee Knoxville, Knoxville, USA
[d]Neutron Scattering Division, Oak Ridge National Laboratory, Oak Ridge, USA
[e]McKelvey School of Engineering, Washington University in St. Louis, St. Louis, USA
[f]Bredesen Center for Interdisciplinary Research and Education, University of Tennessee Knoxville, Knoxville, USA
[*]Corresponding author. Email: yangg@ornl.gov
[†]These authors contributed equally to this work.

1 Experimental Details

1.1 Electrolyte and Cathode Sheet Fabrication

A composite slurry was formulated by blending poly(isobutylene) (average MW $\approx$ 1270 kg mol^{-1}) with LPSCl powder (d_{50} = 5 μm) at a mass ratio of 5:95. The slurry composition comprised 54 wt% solids dispersed in 46 wt% toluene. This mixture was ball-milled using zirconia media at low rotational speed for 18 h to achieve uniform dispersion. Following milling, the slurry was reintroduced into an argon-filled glovebox. The dispersion was then cast onto a non-stick Mylar substrate using the doctor-blade method and allowed to dry under ambient laboratory conditions. The dried film was laminated between two sheets of Mylar and removed from the glovebox for densification. Cold rolling (MTI cold roller press, MSK-HRP-MR100DC) was performed at room temperature (25 °C), gradually reducing film thickness through multiple passes using increasing shim gaps. The entire calendaring process was carried out inside an airtight sealed pouch. The

densified sheets were immediately returned to the glovebox and vacuum-dried overnight to eliminate any residual solvent. The composite cathode was produced via a dry-mixing route inside an argon atmosphere. The formulation included $LiNbO_3$-coated NMC811 as the active material, LPSCl as the solid electrolyte, vapor-grown carbon fibers (VGCF) as conductive additive, and PTFE as a binder, in a weight ratio of 80:16:3:1. The dry blend was manually rolled into a cohesive film using a cylindrical roller. Discs of 6 mm diameter were then punched from the rolled film to serve as cathode electrodes.

1.2 Silicon Anode Preparation

Micron-sized silicon powder (µm-Si, Alfa Aesar) and polyvinylidene fluoride (PVDF) binder were mixed in an N-methyl-2-pyrrolidone (NMP) solution at a 99.9:0.1 weight ratio. The binder content was maintained at 0.1 wt%, and the mixture was continuously stirred for 24 h using a magnetic stirrer to ensure homogeneity. The resulting slurry was coated onto copper foil using a doctor blade to achieve a uniform film. The coated foil was initially dried at 70 °C on a hotplate and subsequently placed in a vacuum oven at 80 °C for 2 h to remove residual NMP. Electrode discs of 6 mm diameter were then punched from the dried film.

1.3 Cell Assembly for Neutron Imaging

A custom-designed in-operando cell assembly was employed for neutron imaging measurements. The cell mold consisted of a PTFE housing (4 mm diameter), two stainless steel plungers, and an external frame to apply mechanical pressure during operation. The stainless steel plungers and the PTFE casing are relatively transparent to neutrons, so they are brighter compared to the electrodes and electrolyte at the center. Two electrolyte discs (∼4 mm in diameter) were stacked and compressed under a pressure of 3 MPa to form the LPSCl electrolyte layer. The cell was assembled with an N/P ratio of 1.1, maintained consistently throughout testing. The composite cathode was then placed on one side of the electrolyte, and a carbon-coated aluminum foil served as the current collector. The silicon anode was positioned on the opposite side. The complete stack was cold-pressed at 470 MPa for 3 min and then secured to maintain a constant stack pressure of 30 MPa during electrochemical operation.

1.4 Electrochemical Cycling and Neutron Imaging

Galvanostatic cycling was conducted within a voltage window of 2.6–4.3 V. Cells were tested under two current density conditions: 0.5 mA cm^{-2} (C/10 rate) and 1.0 mA cm^{-2} (C/5 rate) to assess performance under low and moderate loads, respectively. Neutron imaging was performed at the CG1D cold neutron beamline at the High Flux Isotope Reactor, Oak Ridge National Laboratory [1, 2]. The polychromatic cold neutron beam spanned wavelengths of 0.8–6 Å, with a peak flux of 2.2×10^6 n cm^{-2} s^{-1} at 2.6 Å. A pinhole of 11 mm diameter and a sample-to-detector distance of 6.59 m enabled spatial resolution of approximately 25 µm. Transmitted neutrons were captured by a scientific CMOS (sCMOS) detector (QHY600) coupled to a 20 µm-thick Gd_2O_2S:Tb scintillator

screen. During in-operando tests, 2D neutron radiographs were acquired at 5-minute intervals for real-time monitoring of internal cell processes.

Fig. 1e) and f) of the manuscript displays the Galvanostatic cycling described in this subsection. The two cycles show above are the basis for the simulations in the manuscript at low and high C-rates, respectively.

2 Processing Neutron Data

2.1 Assessing Li Concentration Changes based on Neutron Radiography

The output from the neutron imaging experiment is a series of grayscale transmissions. A significant number of assumptions and calculations must be made in order to estimate the lithium concentration changes in the cathode as a function of time.

The transmission, T, is defined as the correlation between the incident, I_0, and transmitted, I, neutron beams. By Lambert-Beer law [3, 4], Eq. (S1) can be established:

$$T(x,y) = \frac{I(x,y)}{I_0(x,y)} = e^{-x\mu} \tag{S1}$$

Where x is the average thickness, and μ is the attenuation coefficient, which is a material property. Note that the raw radiographs, $I(x,y)$, are normalized by the open-beam (flat field) images $I_0(x,y)$ to remove beam non-uniformity, detector grain variations, and fixed-pattern structures. The thickness, x_i, is different for every pixel i, since the PTFE casing is a cylinder.

For a composite cathode, each element will have a different attenuation coefficient, and therefore Eq. (S1) can be re-written as:

$$T = e^{\sum_i -x_i\mu_i} \tag{S2}$$

where μ_i is the attenuation coefficient of element i. The attenuation coefficient of each element can be estimated as follows:

$$\mu_i = \sigma_i \frac{\rho_i N_A}{M} \tag{S3}$$

where σ_i is the neutron cross-section of element i, ρ_i is the density of element i, M is the molar mass, and N_A is Avogrado's constant. Combining Eq. (S3) with Eq. (S2), it is clear that the interaction of a certain element with the neutron beam is dependent on σ_i and the molar concentration c_i.

For simplification, consider all the elements/components presented along an arbitrary beam path as a whole. Then the pixel value of such projected beam path is $\mu_0 x_i$ at the initial state. At time t, the pixel value would become $\mu_t x_i$. Note that in each pixel, x_i varies due to different length of beam path going through the cylindrical cell. To normalize this geometric variation, one can use the operando image stack to divide the initial image. Therefore, each pixel would only contain the relative changes in attenuation coefficient μ_t/μ_0. Because Li redistribution is the dominating factor

that contributes to the changes in attenuation coefficient, μ_t/μ_0 is used in this work to visualize the relative changes of Li concentration in each pixel with respect to the initial stage.

Lithium has a thermal neutron cross-section of 71 barns [5], so it has a higher contribution towards the attenuation of the transmitted beam compared to the other elements present in this system. Furthermore, the majority of the battery's capacity can be attributed to the movement of Lithium. We then assume the attenuation coefficient of all elements other than Lithium have minor changes. Image co-registration was performed to align each image in the operando stack to the initial images.

Combining all assumptions, the change in concentration can be related to a ratio of transmissions at a pristine state and at a time t by Eq. (S4)

$$\frac{T_t}{T_0} = e^{-x\sigma N_A \Delta c_{Li}} \tag{S4}$$

Negative natural logarithm was applied to all the aligned images to convert the pixel values from transmission (T) to $\sum_i \mu_i x_i$. By applying this transformation to Eq. S4, the following expression can be obtained:

$$\Delta c_{Li} = \frac{-\ln \frac{T_t}{T_0}}{x\sigma N_A} \tag{S5}$$

For transmission values averaged along the radial direction, we used the average thickness of the circular cross section, $x = 1/2\pi r$, with $r = 2mm$.

Finally, to actually quantify the change in Lithium, an estimate of the Lithium content in the pristine state is needed. The active material particles are assumed to deplete Li, but the Li in the LPSCl is not available. Thus, with a mass loading of 30 mg/cm^2, and knowing the dimensions of the cathode, the mobile Li concentration is estimate to be 2.0572×10^4 mol/m^3.

The change in concentration Eq. (S5) can then be expressed as a percent change in concentration when normalized by the estimate of initial concentration. Furthermore, each slice is a 5-point moving average of the surrounding slices. This effectively minimizes sharp spikes (noise) from the imaging process.

2.2 Beam Hardening Effects

Beam hardening was evaluated by measuring similar battery samples at both VENUS, a new time-of-flight imaging beamline and MARS and compared. The advantage of measuring at VENUS is that a small wavelength portion of the data can be considered as monochromatic and thus, after cylindrical geometry correction, beam hardening can be assessed. For the VENUS monochromatic evaluation, we chose neutron radiographs at approximately 0.85 Å$\pm$ 0.05 Å. As seen in Fig. S1, there is no significant difference between VENUS white beam, VENUS monochromatic and MARS white beam:

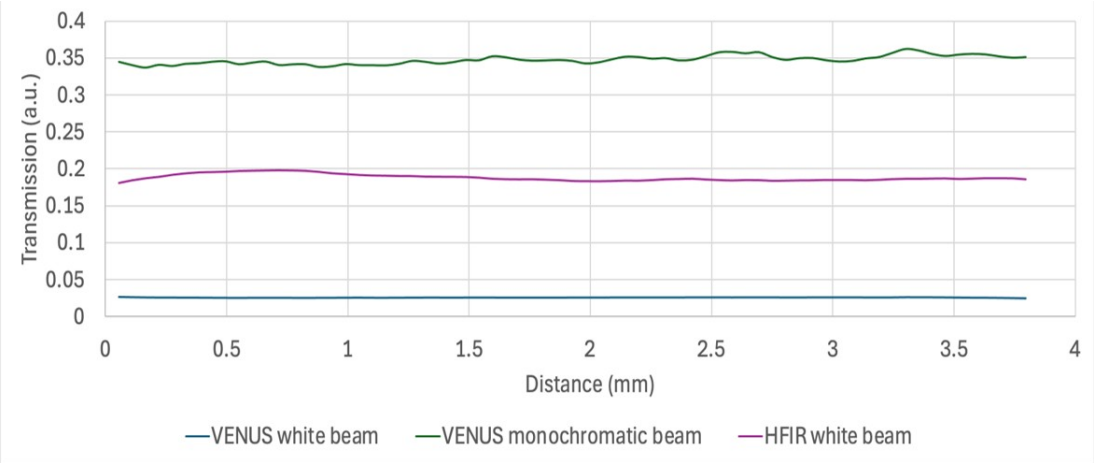

Figure S1: Neutron transmission through battery sample at VENUS and MARS.

Note that all data was first normalized, then corrected for the cylindrical geometry, and finally the profile across each data set was plotted above. Evidently, the VENUS monochromatic plot shows more irregularities due to the lower signal-to-noise than with VENUS and HFIR white beam data, which compromise all neutrons produced by the sources.

3 Galvanostatic Intermittent Titration Technique

It is well know that the diffusion coefficient can substantially change during charge and discharge for an NMC AM particle. Techniques like Galvanostatic Intermittent Titration Technique (GITT) are common [6] to quantify the average diffusion coefficient of Li in active material particles.

However, as observed from the simulation and experiment, there are significant Li concentration gradients within the composite cathode, and as such, we cannot ascribe the same diffusion coefficient to all AM particles. Instead, we generalize the GITT results to fit in the theory of anomalous diffusion [7], which dictates the following:

$$D' = D_{\text{trace}} \frac{c_{\text{Li,max}} + c_{\text{Li}}}{c_{\text{Li,max}} - c_{\text{Li}}} \tag{S6}$$

where D_{trace} is the diffusion coefficient when Li is present in trace amounts, D' is the actual observed diffusion coefficient, c_{max} is the saturation concentration of Li, and c_{Li} is the actual concentration of Li.

The GITT measurement gives the average diffusion coefficient of the cathode at a given SOC. We convert SOC to Lithium concentration based on the neutron imaging data, and then fit D_{trace} and c_{max}, as is shown in Fig. S2.

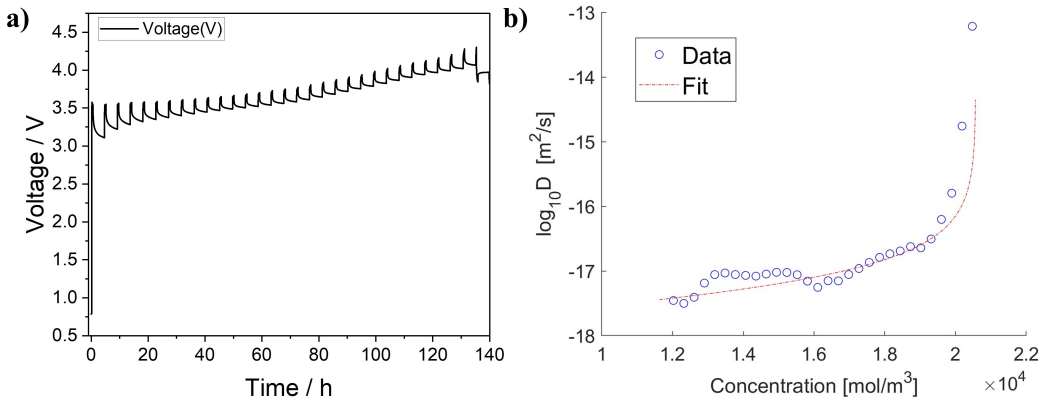

Figure S2: **a)** GITT experimental results from which the average diffusion coefficient is derived. **b)** Utilizing the neutron imaging data and GITT measurements in tandem to fit them to the theory of anomalous diffusion in Eq. S6.

GITT in Fig. 3**a)** was conducted using galvanostatic steps at a 0.1 C charge rate for 10 minutes, followed by a 4-hour relaxation period. This sequence was repeated until the cell reached a fully charged state. The corresponding diffusion coefficients were calculated following recent studies based on the spherical diffusion model [8, 9]. In this work, the diffusion length was taken as the crystallite radius of polycrystalline NMC (0.5 μm), reflecting that the rate-limiting diffusion process occurs within the NMC particles due to the natural grain boundary rather than along the ionic pathways of LPSCl.

Note that the fit in Fig. S2b) is not a perfect fit to the data; instead an assumption is made that the diffusion coefficient obeys the theory of anomalous diffusion, which predicts the asymptotic overshoot in the diffusion coefficient near saturation, while elsewhere it approaches Ficksian diffusion behavior. While there is potential error from the quantification of lithium depletion based on the neutron imaging, the diffusion coefficients measured via GITT represent well the change in diffusion coefficient observed in galvanostatic cycling. Therefore, the theory of anomalous diffusion correlates the two to give some mechanism for the spatially resolved evolution of diffusion coefficient as a function of the local lithium concentration. The importance of this mechanism is illustrated in Fig. S5; without the evolution in diffusion coefficient the simulated depletion significantly overshoots the empirically derived results.

In the absence of the neutron imaging experiment, the authors recommend leveraging the SOC-based GITT results to evolve the diffusion coefficient in simulation. The clear downside of this approach is not having a spatially resolved diffusion coefficient in the cathode, which is clearly necessary due to the local cathode-scale lithium concentration heterogeneity.

4 Simulation Information

This section will outline all of the aspects of the simulation that are relevant to the discussions included in the manuscript. For the interested reader that wants to dive deeper, the code used is available on GitHub[1] along with additional documentation.

4.1 Finite Volume Formulation

The time dependent mass flux can be expressed in terms of Fick's second law as follows:

$$\frac{\partial c_{Li}}{\partial t} = \nabla \cdot (D \nabla c_{Li}) \tag{S7}$$

In this heterogeneous three-phase system, Eq. (S7) is not continuous on domain Ω, since each phase has its own diffusion coefficient. The transition between two phases is thus discontinuous.

However, the equation can be re-written for each control volume, $\bar{\Omega}_{i,j}$, such that $\Omega = \bigcup \bar{\Omega}_{i,j}$, and each $\bar{\Omega}_{i,j}$ belongs to one phase and one phase only.

The discretized finite volume formulation can be written as follows:

$$\int_t^{t+\Delta t} \int_{\bar{\Omega}_{i,j}} \frac{\partial c_{Li}}{\partial t} d\bar{\Omega}_{i,j} dt = \int_t^{t+\Delta t} \int_{\bar{\Omega}_{i,j}} \nabla \cdot (D_{i,j} \nabla c_{Li})\, d\bar{\Omega}_{i,j} dt \tag{S8}$$

where the diffusion coefficient, $D_{i,j}$, is dependent on which phase $\bar{\Omega}_{i,j}$ belongs to. Additionally, note that the values of $D_{i,j}$ are updated depending on local concentration, $c_{i,j}$, according to the theory of anomalous diffusion shown in Eq. (S6), which states that any diffusion coefficient D' is a function of local concentration. Thus, at any $\bar{\Omega}_{i,j}$, $D_{i,j} = D'(c_{i,j})$.

It is clear that now Ω is Lebesgue continuous, and thus Gauss' divergence theorem can be applied to the inner integral on the right-hand side, which simplifies to the following:

$$\int_{\bar{\Omega}_{i,j}} \nabla \cdot (D_{i,j} \nabla c_{Li})\, d\bar{\Omega}_{i,j} = \oint_{\bar{\Omega}_{i,j}} (D_{i,j} \nabla c_{Li}) \cdot \vec{n} d\bar{\Omega}_{i,j} \tag{S9}$$

The volume integral on the left-hand side of Eq. (S8) is a simple evaluation. The time integrals need special attention, and can be approximated as follows:

$$\int_t^{t+\Delta t} c_{Li} dt = (\theta c_{Li} + (1-\theta) c_{Li}^0) \Delta t \tag{S10}$$

Where θ is a constant dependent on the chosen discretization method, and c_{Li}^0 is the known concentration at the previous time step. The Crank-Nicolson method [10] is chosen, with $\theta = 1/2$.

Finally, all values from the integral can be collected in the following format:

$$\mathbf{A}\vec{x} = \vec{b} \tag{S11}$$

Where the vector $\vec{x}$ contains all of the unknown concentrations at time $t + \Delta t$, and the matrix $\mathbf{A}$ is a pentadiagonal matrix (2D simulation) with all of the central differencing scheme constants.

[1] https://github.com/adama-wzr/EffectiveDiffusivityFVM

The right-hand side vector, $\vec{b}$, contains all of the known values and constants from the previous time step, as well as the boundary conditions.

4.2 Time Constraint

While the method is convergent, it does impose a constraint on the time step Δt that is necessary for stability [11], outline in Eq. (S12)

$$\Delta t \leq \frac{\Delta x^2}{D} \tag{S12}$$

where Δx is the control volume side length (here is a synonym of pixel resolution for the FIB-SEM), and D is a diffusion coefficient. It is clear that the faster the diffusion, the higher time resolution Δt is needed for accuracy.

The values for the $D_{Li|AM}$ are a function of concentration, and are derived directly from the GITT data in section 3. The maximum value is in the order of 10^{-14} m^2/s. The diffusion coefficient on the solid state electrolyte (SSE) $D_{Li|SSE}$ is in the order of 10^{-11} m^2/s [12]. Since $D_{Li|SSE}$ is at least 3 orders of magnitude larger than $D_{Li|AM}$, the SSE is excluded from the simulation, and the Li concentration is assumed to be constant in the SSE electrolyte.

This assumption also impacts the time resolution in Eq. (S12), and Δt is three orders of magnitude larger. This constraint means the simulation is effectively three orders of magnitude faster by removing the Li concentration gradient in the SSE. This also doesn't affect the results: the time resolution of the neutron imaging data is roughly 5 minutes per image, so the diffusion phenomena cannot be seen regardless.

4.3 Sub-Domain Filtering

One of the major downsides of relying on FIB-SEM scans for the simulation domain relates to the limitations of the 2D representation of the cathode and potential noise from image processing.

The small AM particle sub-domains can be interpreted in two ways: either it is a larger particle that is in the background of the 2D slice, or it is noise from image processing. Both are equally detrimental to the simulation and are filtered out, as shown in Fig. S3. The particle labeling was done using the ED-cPSD software [13].

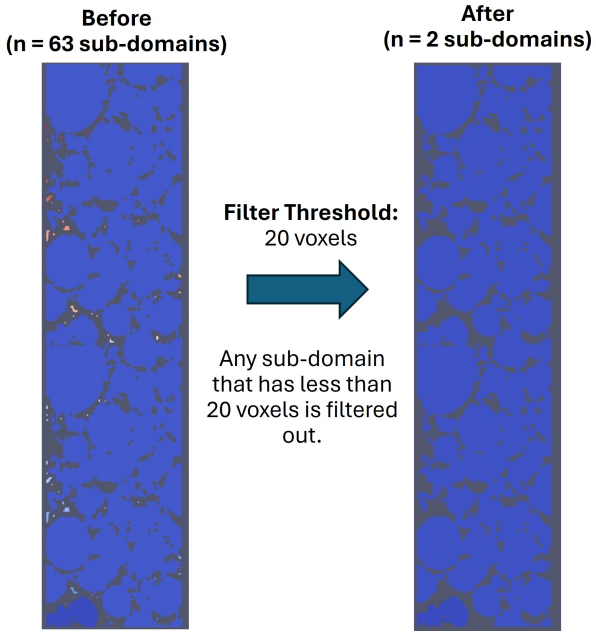

Figure S3: Figure shows the before and after of the applied sub-domain filtering algorithm based on the total volume. The figure on the right-hand side is the one used for all of the simulations in the manuscript.

A flood-fill algorithm is employed to filter out small subdomains. The whole particle domain is left unlabeled, and the algorithm procedurally scans the entire domain. Once an unlabeled particle is found, it receives a label, and all directly connected particles receive the same label.

Once the algorithm labels the whole connected domain, it continues the procedural scan for other unlabeled particles. When a new unlabeled particle is found, it is clear that this particle is not connected to any of the labeled domains, and thus receives a new label. This algorithm does two things: if finds the number of sub-domains, and it calculates the volume of the sub-domain.

The majority of sub-domains are less than twenty particles in volume, and after the filtering step, the cathode is represented as only two AM particle sub-domains. Both domains are fully connected.

4.4 Tortuosity Calculation

The tortuosity calculation is a special case in the solution of the Laplace equation for a single phase. In short, a medium with porosity ϵ and diffusion coefficient D has a theoretical maximum effective diffusivity of

$$D_{\text{eff,max}} = \epsilon D \tag{S13}$$

If Eq. S13 was used to describe a bundle straight tubes, then the effective diffusivity would be the same as the theoretical maximum. However, if the tubes are not straight, the effective diffusive length is necessarily larger than the straight line case, hence resulting in a lower effective diffusivity. Manipulating Eq. S13, one can obtain the following expression for tortuosity:

$$\tau = \frac{D \cdot \epsilon}{D_{\text{eff}}} \tag{S14}$$

where in Eq. S14, D_{eff} is the calculated effective diffusivity via the finite volume method. It is also obvious that $\tau \geq 1$, and the case where $\tau = 1$ represents a bundle of straight tubes. We note that the tortuosities are geometric parameters, and therefore do not depend on the diffusion coefficient. Thus, D is a constant and arbitrary for tortuosity simulations. The tortuosities calculated are also assumed to be constant, since the cathode does not experience significant deformation in one cycle. More discussion on the topic can be found in Cooper et al. [14].

In this work, two tortuosities are of interest: the tortuosity of electron diffusion pathways within the AM, and tortuosity in Li-ion diffusion in the SE. Both of those were simulated directly on the same representative volume, the results of which can be seen in Fig. S4

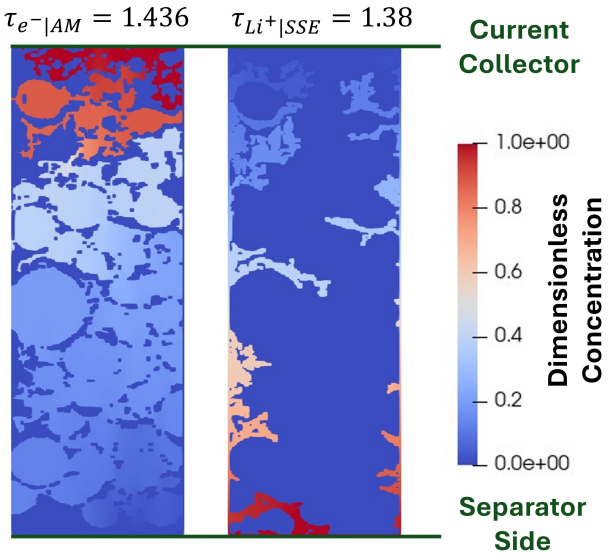

Figure S4: Figure shows the results of tortuosity calculation for the electrons in the active material phase and for the Li-ion in the solid electrolyte phase. The tortuosity was calculated directly based on the results from the finite volume simulation.

4.5 Implementation and Solution

The code implementation is done in C++ and CUDA. In testing, GPU computing is often hundreds of times faster than CPU computing, and thus it is the only practical way of simulating hours worth of charge and discharge cycles with a time resolution of less than one second.

A GPU kernel solves the standard over-relaxed version of the Jacobi iteration, with weight $w = 2/3$. For each time-step, the convergence is based on the percent change of the new concentration distribution versus the concentration distribution 100 iterations ago. The iterative solver continues until the average percent change is less than 10^{-4} or the maximum number of iterations, set to 10^6.

4.6 Summary of Simulation Parameters

Some parameters are common between the simulation at high and low current densities, especially parameters that deal with the geometry. These parameters are outlined in Table S1. Other parameters that depend on the experimental setup, and therefore are specific to each simulation, are included in Table S2.

Parameter	Value	Units
$\tau_{\mathrm{Li^+}\vert\mathrm{SSE}}$	1.380	-
$\tau_{\mathrm{e^-}\vert\mathrm{AM}}$	1.436	-
Resolution	270.0	nm/pixel
c_0	2.0572×10^4	mol/m^3
$c_{\max}$	2.057225×10^4	mol/m^3
D_{trace}	10^{-18}	m^2/s
Capture Time	302.5	seconds/frame

Table S1: The values outlined in this table are simulation parameters that are common to the simulation at high and low C-rates.

Parameter	High C-Rate	Low C-Rate	Units
Current Density	1	0.5	mA/cm^2
Charge Time	12705.0	46885.0	s
Total Time	21477.5	78950.0	s

Table S2: The values outlined in this table are simulation parameters that dependent on the experimental setup, and therefore are dependent on the C-rate.

For the two simulations that do not have any corresponding validating neutron radiographs (Figure 5 in the manuscript), the values for the charge time and discharge time were extrapolated from the experimental data. This data is displayed in Table S3

Parameter	C/25	C/8.3	Units
Current Density	0.2	0.6	mA/cm^2
Charge Time	117370.0	22082.5	s
Total Time	198440.0	37510.0	s

Table S3: The values outlined in this table are simulation parameters that are extrapolated from the experimental parameters collected and used in table S2.

The only other adjustment needed relates to the simulation at C/25; the interfacial flux was too small, and therefore the effects of the anomalous diffusion were not appropriately felt near 100% SOC. Therefore, for this simulation alone, the c_{max} was adjusted from 2.057225×10^4 mol/m^3 to 2.05723×10^4 mol/m^3. This adjustment only affects concentrations near saturation at 100% SOC.

5 Simulation Rationale

In the manuscript, the total flux from AM-SE through active interfaces is given by Eq. (S15):

$$J^*(t) = \sum_{i,j}^{N} W_{i,j} \frac{I_0}{z\, F \sum_{i,j}^{N} s_{i,j}} \tag{S15}$$

Each active interface has a flux that is unique, and this flux is both a function of time and location. The local flux, which is the applied boundary condition in each active interface with coordinates i, j, is calculated as in Eq. (S16).

$$J^*_{i,j}(t) = W_{i,j} \frac{I_0}{zFs_{i,j}} \tag{S16}$$

With the term $W_{i,j}$ being broken down as $W_{i,j} = w_1 \cdot w_2$, where w_1 and w_2 are given as follows:

$$w_1(y) = 2\left[1 - \frac{\left(\tau_{e^-|AM} \cdot d_{cc} - \tau_{Li^+|SE} \cdot d_{SE}\right)^2}{\left(\tau_{max} H\right)^2}\right] \tag{S17}$$

$$w_2(x, y, t) = \sqrt{\frac{c_{i,j}(t)}{c_{sat}}} \tag{S18}$$

The term w_1 is a geometric term, related to the tortuosity in conduction pathways away from the active interface, and w_2 is a commonly used term of concentration dependence [15]. In this section, the effects of each term will be studied by eliminating them from the simulation.

Like stated in the manuscript, Eq. S17 is a penalty factor that accounts for the geometry of the composite cathode, and is applied to the reaction rates observed in the AM-SE active interfaces. The terms $\tau \cdot d$ measure the expected diffusion length. d_{cc} and d_{SE} are the straight line distances from the active interface to the current collector and the solid electrolyte, respectively, such that $d_{cc} + d_{SE} = H$, where H is the cathode height. The tortuosity is a dimensionless adjustment factor to the distance; for an arbitrary electron in the cathode, the travel distance towards the current collector will be $\tau_{e^-|AM} \cdot d_{cc}$.

The two boundary cases are at the edges of the cathode: when $d_{cc} \approx 0$, then d_{SE} reaches its highest value. The opposite is true when $d_{SE} \approx 0$. These extremes are clearly penalized based on the data collected from neutron imaging. First, we normalize the distances traveled by the maximum possible distance, $\tau_{max} H$, where H is the height of the cathode and τ_{max} is the highest tortuosity between $\tau_{e^-|AM}$ and $\tau_{Li^+|SE}$.

The power of two is added to both numerator and denominator to avoid negative numbers, and we take the complement of this expression, since it is a penalty factor. Thus, when the numerator is balanced ($\tau_{e^-|AM} \cdot d_{cc} \approx \tau_{Li^+|SE} \cdot d_{SE}$), the penalty factor is near zero. When one of them is clearly larger than the other, then we see a significant penalty. Finally, to conserve the overall mass flux, we need the factor of 2 for the whole expression, since only penalties have been applied.

The final expression for w_1 yields a relationship that promotes higher than expected depletion rates in the center of the cathode, while the edges see significantly less lithium utilization during

charge. This expression is consistent with what we observe from the operando neutron imaging experiment.

5.1 Charge Mechanism

Fig. S5 provides examples of the effect of certain parameters on the simulation result during charge.

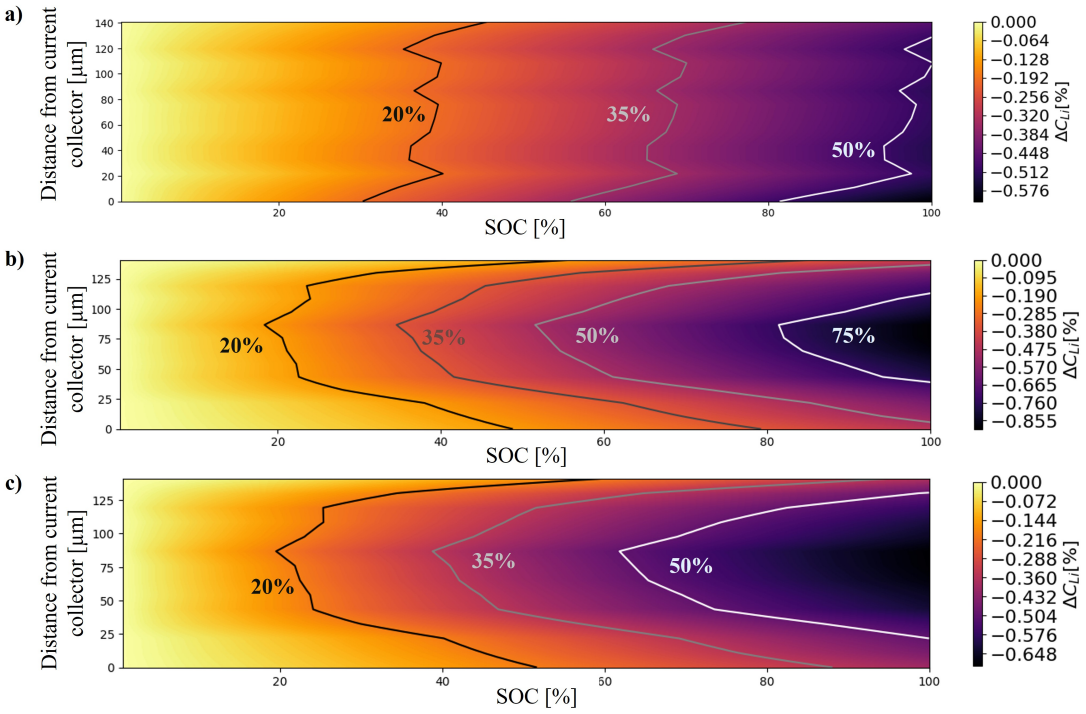

Figure S5: **a)** Baseline simulation not accounting for $W_{i,j}$ in Eq. (S15). **b)** Baseline simulation only introducing w_1, as Eq. (S17). **c)** Baseline with w_1 and w_2, but without the particle filtering and GITT.

Fig. S5**a)** is the simplest possible model, with an even distribution of the source parameter based only on surface area. In this case, local regions with higher than normal surface area to volume ratio have higher depletion, as that is the only factor impacting the flux in Eq. S15. This benchmark yields no similarity to the charge profile in Fig. S6**a)**, but it does yield a similar average lithium depletion. Fig. S5**b)** introduces w_1 to the simulation, which causes the Li concentration profiles to acquire the correct shape. However, since there is no regulatory factor on the rate, this simulation overshoots the Li depletion. Fig. S5**c)** introduces a term that is commonly found in literature [15, 16] to regularize the reaction rate based on the Li availability at the interface. While **c)** yields much better agreement with the neutron imaging data, it still overshoots the delithiation by roughly 10%.

Two issues are identified: first, the simulations above do not adapt the diffusion coefficient based on state of charge or concentration, and instead use the diffusion coefficient at a pristine state. Second, the simulation domain contains "trace" particles from the image processing. Those are

extremely small particles in a scale of less than a μm in diameter, which are either attributed to noise in the imaging, or they could be the tip of large particles hidden in the background. This is an inherent limitation of the 2D approach.

Both issues result in the same problem: the Li concentration in the active interface is overestimated, hence leading to a larger w_2 in Eq. (S18) since $c_{i,j}$ is larger than it should be. The diffusion coefficient issue is addressed in Sec. 3, and the small-particle filtering is addressed in sub-section 4.3, resulting in the simulation shown in Fig. S6**b)**.

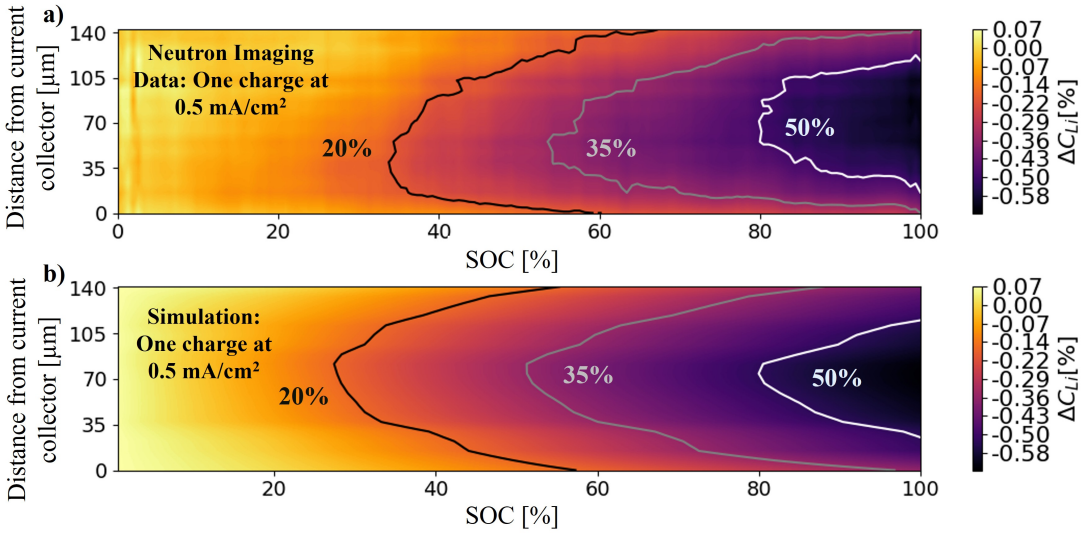

Figure S6: **a)** Neutron imaging data for Li concentration profiles on the cathode during charge at C/10. **b)** Complete simulation of the charge Li concentration profiles using Eq. (S15), diffusion correction based on GITT, and sub-domain filtering.

With all modifications made, this model matches the data collected in the neutron imaging experiment almost exactly for the charge cycle, with a comparison shown in Fig. S6. The peaks in Fig. S6**b)** match the ones from Fig. S6**a)** in shape and size, especially at 35% and 50% depletion rates. At 100% SOC, the average depletion is only 2% larger for the model, which overshoots the depletion near the current collector.

5.2 Discharge Mechanism

The tortuosity dependence does not play a role for discharge. Instead, a relationship using the complement of w_2 is employed, since in discharge the Li will primarily deposit on the most vacant sites. This agrees with the physical phenomena observed via the operando neutron imaging experiment, where the tortuosity dependent reaction rate observed during charge is not observed during discharge.

For this system, this implies the Li will deposit in the locations with the largest vacancies first. When the concentration profile along the length of the cathode is roughly even, Li appears to plate evenly. In other words, Lithiation naturally follows a similar pattern as stripping.

In the case with rate C/10, Li is able to reach a uniform concentration distribution the end of discharge, termed the synchronous behavior. At a rate of C/5, the concentration distribution is not uniform, and thus we claim the cathode is asynchronous in both charge and discharge.

5.3 Error Estimation

Experimental time-dependent lithium concentrations can be compared to the simulated results. The relative error, RE, is calculated as follows:

$$\mathrm{RE} = \frac{\Delta c_{Li,exp} - \Delta c_{Li,sim}}{\Delta c_{Li,exp}} \tag{S19}$$

Please note that the changes in Lithium in the cathode are negative (i.e. no lithium can be added beyond the saturated pristine state). Thus, according to Eq. S19 a positive relative error means the simulation underestimates the amount of lithium present, and a negative value of relative error means the model is overestimating the lithium presence. A spatial distribution of the relative error is shown in Fig S7, which can be obtained by comparing Figs. 3a) and 3b) in the manuscript.

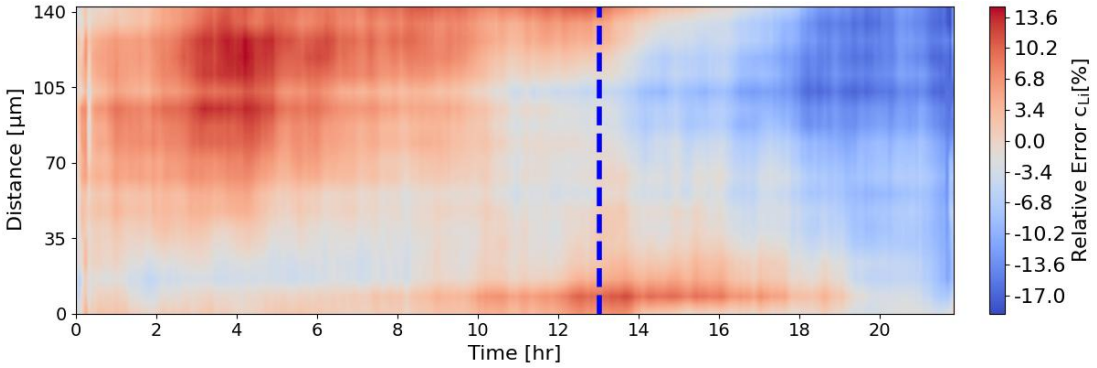

Figure S7: Spatial distribution of the relative error in lithium concentration based on the cycle with rate C/5.

The streaking in Fig. S7 is due to the resolution of the neutron beamline, since the delithiation gradients from the simulation are smooth. The spatially resolved error distribution matches the expectation; the simulation agrees well at the end of the charging process, but significant errors arise at the end of discharge due to the unaccounted capacity loss from the anode side. The solution is the most accurate near the center of the cathode (y $\approx$ 70 μm).

Furthermore, we can average the relative error at each time slice to assess how the error evolves of the charge-discharge cycle. This is shown in figure S8.

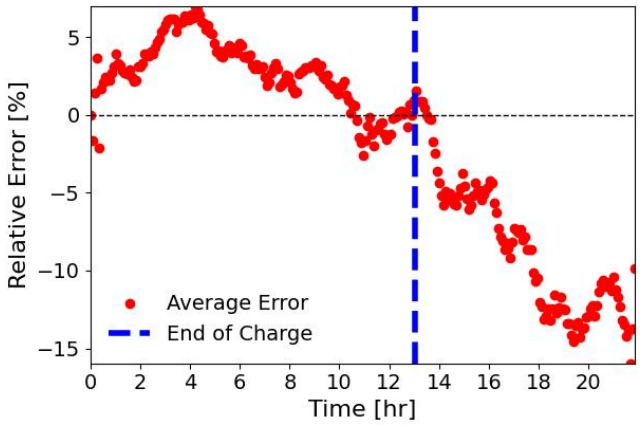

Figure S8: Temporal distribution of the mean relative error in lithium concentration based on the cycle with rate C/5.

The error during charge varies between -2.6% and 6.8%, with the model slightly undershooting the Lithium depletion in the cathode at the middle stages of discharge. The model and data agree well at the end of discharge, not only exhibiting similar depletion amounts (as shown above), but also by exhibiting the same depletion profile (figure 3 in the manuscript).

During discharge, there seems to be linear trend in error going as the depth of discharge increases. This is expected, since we only model the cathode, and hence do not account for any losses that might occur on the anode side. With a Si-based anode, a loss of 15% can be expected on the anode alone. In this work, we observed a capacity loss of 28.4% in the first cycle, suggesting that roughly 13% the capacity loss is due to lithium becoming some interfacial byproduct. The simulation shows a discrepancy of roughly 16% MAE at the end of discharge; thus we attribute the increasing error trend in discharge to not accounting for lithium loss in the anode.

5.4 Transition Time Comparison

The transition time (τ) in electrochemistry is the time taken for the electroactive species to reach a concentration of nearly zero at the surface of the active material, at which point a sharp increase in overpotential is observed. The Sand equation relates the diffusion coefficient in the AM ($D_{Li|AM}$), the applied current density (i), and the bulk concentration of the active species (C^*, lithium in this work), to predict a transition time. The equation is shown below, with n being the number of electrons exchanged, and F being the Faraday constant.

$$i\tau^{\frac{1}{2}} = \frac{1}{2}FnC^*\sqrt{\pi D_{Li|AM}} \tag{S20}$$

The transition time obtained via Eq. S20 is valid for non kinetically limited cathodes[17, 18]. While TWIF-Li is not an electrochemistry model, it is a model for mass transfer, and therefore it is not able to determine the transition time, relying on experimentation to determine cycle times. On the other hand, TWIF-Li allows us to visually see the transition from asynchronous to synchronous delithiation gradients, which usually accompany this transition to a kinetically limited cathode

under higher current densities. The comparison between the experimentally determined and the Sand equation transition times is shown if Fig. S8.

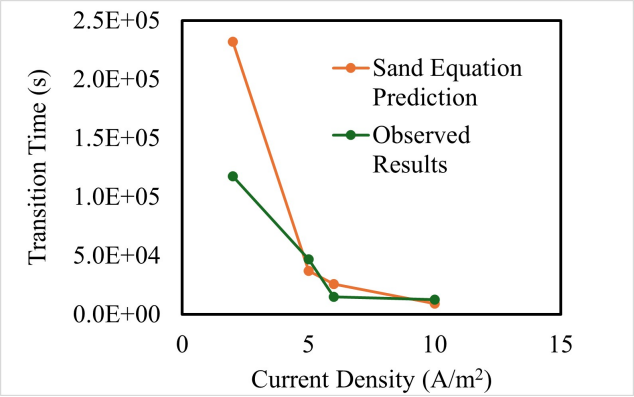

Figure S9: Comparison of transition times based on Sand equation and the experimentally observed transition times.

The trend we observed in the figure is additional evidence to support the claim in the manuscript that the limitation in current density is a kinetic limitation intrinsic to the geometry and chemistry of the cathode, whose asynchronous behavior is exacerbated by higher current densities. In Fig. S9, as the cell becomes kinetically limited beyond C/10, the observed transition time goes beyond the prediction from the Sand equation, which here we theorize it is mainly due to the highly asynchronous lithium profile in the cathode.

6 Mechanistic Insight in Practice

To add some additional experimental evidence to the mechanistic insights from TWIF-Li, identical cells were evaluated with identical cathode compositions but different cathode layer thicknesses. Specifically, the cells were prepared with NMC811 mass loadings of 12 mg cm^{-2} and 25 mg cm^{-2}. The rate capability comparison, the new simulation domain (for the lower loading), and the new lithium distribution profile are included in figure S10.

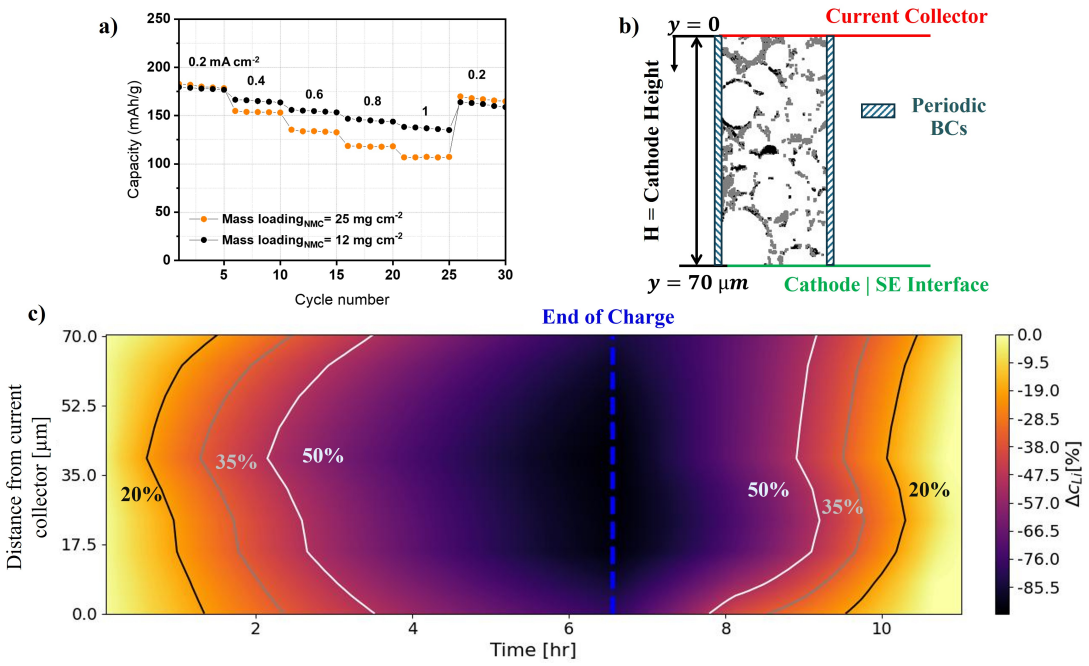

Figure S10: **a)** Rate capability test comparison for two cells with identical cathode composition, but different layer thicknesses. **b)** New cathode geometry is half the size of the geometry in the manuscript. **c)** Simulation of the lithium distribution at C/10 for the lower areal mass loading.

From the rate capability measurements, the cell with approximately half the cathode thickness exhibited a higher specific capacity, indicating improved utilization under practical current densities. When combined with our modeling results, these observations support the key framework prediction that transport limitations and interfacial non-uniformity become more pronounced with increasing cathode thickness. This consistency between experiment and model provides further validation of the proposed TWIF-Li framework.

References

[1] Lowell Crow et al. "The CG1 instrument development test station at the high flux isotope reactor". In: *Nuclear Instruments and Methods in Physics Research Section A: Accelerators, Spectrometers, Detectors and Associated Equipment* 634 (1 Apr. 2011), S71–S74. ISSN: 01689002. DOI: 10.1016/j.nima.2010.06.213. URL: https://linkinghub.elsevier.com/retrieve/pii/S0168900210014038.

[2] Lou Santodonato et al. "The CG-1D Neutron Imaging Beamline at the Oak Ridge National Laboratory High Flux Isotope Reactor". In: *Physics Procedia* 69 (2015), pp. 104–108. ISSN: 18753892. DOI: 10.1016/j.phpro.2015.07.015. URL: https://linkinghub.elsevier.com/retrieve/pii/S1875389215006252.

[3] D. F. Swinehart. "The Beer-Lambert Law". In: *Journal of Chemical Education* 39.7 (July 1962), p. 333. ISSN: 1938-1328. DOI: 10.1021/ed039p333. URL: http://dx.doi.org/10.1021/ed039p333.

[4] Thomas G. Mayerhöfer, Susanne Pahlow, and Jürgen Popp. "The Bouguer-Beer-Lambert Law: Shining Light on the Obscure". In: *ChemPhysChem* 21.18 (Aug. 2020), pp. 2029–2046. ISSN: 1439-7641. DOI: 10.1002/cphc.202000464. URL: http://dx.doi.org/10.1002/cphc.202000464.

[5] Varley F. Sears. "Neutron scattering lengths and cross sections". In: *Neutron News* 3.3 (Jan. 1992), pp. 26–37. ISSN: 1931-7352. DOI: 10.1080/10448639208218770. URL: http://dx.doi.org/10.1080/10448639208218770.

[6] Jeffrey S. Horner et al. "Electrochemical Modeling of GITT Measurements for Improved Solid-State Diffusion Coefficient Evaluation". In: *ACS Applied Energy Materials* 4 (10 Oct. 2021), pp. 11460–11469. ISSN: 25740962. DOI: 10.1021/ACSAEM.1C02218/SUPPL_FILE/AE1C02218_SI_001.PDF. URL: https://doi.org/10.1021/acsaem.1c02218.

[7] P. E. Bakeman and J. M. Borrego. "The Theory of Anomalous Diffusion in Solids Near Diffusant Saturation Concentrations: Example-Phosphorus in Silicon". In: *Journal of The Electrochemical Society* 117 (5 1970), p. 688. ISSN: 00134651. DOI: 10.1149/1.2407605. URL: https://iopscience.iop.org/article/10.1149/1.2407605.

[8] Yuanshun Li et al. "Integrated electro- and chemical characterization of sulfide-based solid-state electrolytes". In: *Materials Advances* 5.23 (2024), pp. 9138–9159. ISSN: 2633-5409. DOI: 10.1039/d4ma00619d. URL: http://dx.doi.org/10.1039/D4MA00619D.

[9] Yuanshun Li et al. "Promising performance of sulfide catholytes compared to halide alternatives in NMC811 cathodes for sheet-type sulfide solid-state batteries". In: *Energy Storage Materials* 80 (July 2025), p. 104385. ISSN: 2405-8297. DOI: 10.1016/j.ensm.2025.104385. URL: http://dx.doi.org/10.1016/j.ensm.2025.104385.

[10] J. Crank and P. Nicolson. "A practical method for numerical evaluation of solutions of partial differential equations of the heat-conduction type". In: *Mathematical Proceedings of the Cambridge Philosophical Society* 43 (1 1947), pp. 50–67. ISSN: 14698064. DOI: 10.1017/S0305004100023197.

[11] H Versteeg and W Malalasekera. *An introduction to computational fluid dynamics*. en. Philadelphia, PA, Feb. 2007.

[12] Ruth Schlenker et al. "Structure and Diffusion Pathways in Li 6 PS 5 Cl Argyrodite from Neutron Diffraction, Pair-Distribution Function Analysis, and NMR". In: *Chemistry of Materials* 32 (19 Oct. 2020), pp. 8420–8430. ISSN: 0897-4756. DOI: 10.1021/acs.chemmater.0c02418. URL: https://pubs.acs.org/doi/10.1021/acs.chemmater.0c02418.

[13] A. Adam et al. "ED-cPSD: Fast Phase-Size Distribution via Sequential Erosion-Dilation". In: *SoftwareX* 31 (Sept. 2025). ISSN: 23527110. DOI: 10.1016/j.softx.2025.102211.

[14] S. J. Cooper et al. "TauFactor: An open-source application for calculating tortuosity factors from tomographic data". In: *SoftwareX* 5 (Jan. 2016), pp. 203–210. ISSN: 2352-7110. DOI: 10.1016/J.SOFTX.2016.09.002.

[15] Allen J.. Bard and Larry R.. Faulkner. *Electrochemical methods : fundamentals and applications*. John Wiley & Sons, Inc., 2001, p. 833. ISBN: 0471043729.

[16] Nikhil Sharma et al. "Asynchronous-to-Synchronous Transition of Li Reactions in Solid-Solution Cathodes". In: *Nano Letters* 22 (14 July 2022), pp. 5883–5890. ISSN: 15306992. DOI: 10.1021/ACS.NANOLETT.2C01818/SUPPL_FILE/NL2C01818_SI_003.MP4. URL: /doi/pdf/10.1021/acs.nanolett.2c01818?ref=article_openPDF.

[17] Lukas Stolz et al. "The Sand equation and its enormous practical relevance for solid-state lithium metal batteries". In: *Materials Today* 44 (Apr. 2021), pp. 9–14. ISSN: 18734103. DOI: 10.1016/j.mattod.2020.11.025.

[18] Lukas Stolz et al. "Kinetical threshold limits in solid-state lithium batteries: Data on practical relevance of sand equation". In: *Data in Brief* 34 (Feb. 2021), p. 106688. ISSN: 23523409. DOI: 10.1016/j.dib.2020.106688. URL: https://linkinghub.elsevier.com/retrieve/pii/S2352340920315675.